Nanoscale Advances

ROYAL SOCIETY OF CHEMISTRY

PAPER

View Article Online
View Journal

Cite this: DOI: 10.1039/d5na01164g

Photochemical processes developed in composites based on MoS_2, poly(*ortho*-toluidine), and reduced graphene oxide

Madalina Cercel,[ab] Andreea Nila,[b] Ion Smaranda,[b] Andreea Androne,[b] Teodora Burlanescu,[b] Adam Lörinczi,[b] Catalin Negrila,[b] Elena Matei[b] and Mihaela Baibarac *[b]

Using solid-state interactions, composites based on molybdenum disulfide (MoS_2), poly(*ortho*-toluidine) (POT), and reduced graphene oxide (RGO) were prepared. Raman scattering and FTIR spectroscopic studies have demonstrated that the interaction of the RGO and MoS_2 sheets with the POT-emeraldine base state (EB) leads to composites composed of RGO sheets non-covalently functionalized with pseudo-protonic POT doped with MoS_2 and RGO covalently functionalized with POT-leucoemeraldine salt (LS). An alternative way to prepare these composites is the solid-state interaction of the RGO and MoS_2 sheets with the POT-emeraldine salt (ES), resulting in composites composed of RGO non-covalently functionalized with POT-salt having pseudo-protonic acidic entities doped with MoS_2 and RGO covalently functionalized with POT-leucoemeraldine base (LB). Using UV-Vis spectroscopy, we demonstrate that the exposure of these composites to UV light in protic polar solvents leads to the generation of partially de-doped POT-LB and POT-ES. The features of the composites after light exposure, as well as their transformation to the salt state, are highlighted by surface-enhanced Raman scattering. This study contributes to better understanding of the properties of the composites based on MoS_2, POT, and RGO, highlighting the need to avoid the exposure of composites dissolved in polar protic solvents to UV light.

Received 25th December 2025
Accepted 22nd May 2026

DOI: 10.1039/d5na01164g

rsc.li/nanoscale-advances

1. Introduction

In the last ten years, special attention has been paid to binary and ternary composites containing transition metal dichalcogenides, such as MoS_2 and WS_2, reduced graphene oxide (RGO), and conducting polymers.[1–3] The main targeted applications of these composites are in the fields of (i) supercapacitors,[4] (ii) rechargeable lithium batteries,[5] (iii) rechargeable sodium batteries,[6] (iv) aptasensors for the detection of aflatoxin B1,[7] (v) electrochemical sensors for the simultaneous detection of ascorbic acid, dopamine, and uric acid,[8] (vi) layers in OLEDs,[9] (vii) Li–S batteries,[10] (viii) immunosensors,[11] and (ix) photocatalysis as antipollution and antimicrobial agents.[12] The most commonly used polymers for the preparation of these composites are polypyrrole[5] and polyaniline.[4] The first work on composites based on poly(*o*-toluidine) (POT) and MoS_2- and WS_2-type TMDs was reported in 2025.[3] Since POT is a polyaniline that has benzene and quinoid rings substituted with a methyl group, in the following, we will review the main methods used for the synthesis of MoS_2/PANI/RGO composites. Four methods are used to obtain ternary composites of the MoS_2/PANI/RGO type. (i) Hydrothermal synthesis of MoS_2 in the presence of graphene oxide (GO) results in the MoS_2/RGO composite, followed by the *in situ* polymerization reaction of aniline in the presence of HCl and ammonium persulfate (APS).[4] (ii) Polymerization of aniline in the presence of APS, exfoliated graphene and MoS_2 leads to the formation of PANI/graphene/MoS_2 composites with intercalated structures of graphene and MoS_2 layers encapsulated in PANI.[13] (iii) Hydrothermal synthesis of the MoS_2/RGO binary composite and the subsequent chemical polymerization of aniline in the presence of the MoS_2/RGO binary composite using APS as an oxidizing agent results in a ternary MoS_2/RGO/PANI composite, in which the PANI concentration can vary between 50 and 80 wt%; PANI adsorption on the surface of the MoS_2/RGO binary composite occurs through electrostatic interactions established between the structure of the MoS_2/RGO composite and PANI.[14] (iv) 3D MoS_x-PANI@RGO composites can be prepared by the hydrothermal method. To achieve these, GO is used as a precursor for RGO, which acts as a catalyst for the synthesis of MoS_x nanoparticles as well as an acidic dopant for the PANI-

[a]University of Bucharest, Faculty of Physics, Atomistilor Street 405A, Magurele, Romania

[b]National Institute of Materials Physics, Laboratory of Optical Processes in Nanostructured Materials, Atomistilor Street 405A, Magurele, Romania. E-mail: barac@infim.ro

Table 1 Comparative analysis of the MoS_2/RGO/conducting polymer composites

Composite, ref.	Polymer	Synthesis method	Main topic	Key limitation
MoS_2/RGO/PANI[4]	PANI	Hydrothermal and *in situ* polymerization	Supercapacitor performance	Limited interfacial analysis
Graphene/MoS_2/PANI[13]	PANI	Chemical polymerization using exfoliated phases	Electrode materials	Morphology/performance
MoS_2/RGO/PANI[14]	PANI	Hydrothermal and oxidative polymerization	Electrochemical behavior	Weak insights into interactions
MoSx/PANI@RGO[15]	PANI	Hydrothermal (3D aerogel)	Energy storage	No detailed spectroscopic correlation
MoS_2/GNP/PANI[18]	PANI/PPY	Melt + exfoliation	Supercapacitors	Application-driven
MoS_2/GNP/PANI[5]	PANI/PPY	Melt + exfoliation	Supercapacitors	Application-driven
CNT/PANI@MoS_2 (ref. 19)	PANI	Hydrothermal	Structure–property	No RGO
PANI/MoS_2 (ref. 20)	PANI	Hydrothermal	Adsorption	Binary system
PANI/MoS_2 (ref. 21)	PANI	Mixture	Supercapacitors	No RGO
PANI/RGO[22]	PANI	Chemical/electrochemical polymerization	Supercapacitors	No MoS_2
POT/MoS_2:WS_2 (ref. 3)	POT	Mixture	Electrical properties	No RGO
POT/RGO[23]	POT	Solid-state reaction	Supercapacitors	No MoS_2
MoS_2/RGO/POT [this work]	POT	Solid-state reaction	Interfacial interactions and photochemical behavior	MoS_2/RGO/POT

emeraldine base.[15] Compared with these processes, in this work, for the preparation of the MoS_2/POT/RGO composites, solid-state interactions are used, and POT is used as both an emeraldine base (EB) and an emeraldine salt (ES). In this context, it should be mentioned that like PANI, POT in the semiconducting state can exist in three forms, known as leucoemeraldine base (LB), emeraldine base (EB) and pernigranilane base (PB). The difference between these forms is in the number of structural units present: (a) LB contains four benzene rings and four amine groups; (b) EB contains three benzene rings, a quinoid ring, two amine groups and two imine groups; and (c) PB contains two benzene rings, two quinoid rings and four imine groups. The conductive forms of POT are known as leucoemeraldine salt (LS), emeraldine salt (ES), and pernigranilane salt (PS).[16,17] They are characterized by the presence of protonated or pseudo-protonic structures. The transition from the semiconducting to conducting state of POT can be achieved similarly to PANI by (a) acidic protonic doping, which involves the use of an acid, such as H_2SO_4 and HCl, with the generation of the protonated structure on the macromolecular chain; (b) redox doping, which involves reactions in which the dopant moves or brings electrons from or to the conducting polymer, leading to a p- or n-type doping; and (c) pseudo-acidic protonic doping, which takes place in the presence of organic or inorganic salts such as tetrabutylammonium tetrafluoroborate and heavy metal sulfides.[16,17] Although important progress has been reported in the case of MoS_2/PANI/RGO composites, little information is available on the chemical interactions that take place at the interface of the three constituents, which may have important consequences on the physicochemical properties and, implicitly, on the applications envisaged for such materials. In this work, a detailed understanding of the interactions that take place during the preparation of the composites composed of MoS_2, RGO, and POT will be presented through correlated studies of X-ray diffraction (XRD), Raman scattering, FTIR spectroscopy, and UV-Vis spectroscopy. The behavior of these composites in the presence of polar and nonpolar solvents, as well as light emitted by a halogen source, will also be reported. To highlight the photochemical reaction products of binary and ternary composites, SERS studies are presented.

To the best of our knowledge, no studies have reported MoS_2/RGO/POT ternary composites prepared *via* solid-state interactions or have provided a detailed spectroscopic investigation of the interfacial interactions and photochemical behavior of such systems. A comparative analysis of the progress reported on MoS_2/RGO/conducting polymer composites is shown in Table 1. Considering this progress, the novelty of the present study can be outlined more clearly as follows:

(i) Although a significant number of studies have been devoted to MoS_2/RGO composites incorporating conducting polymers such as polyaniline (PANI) and polypyrrole (PPY), the use of poly(*o*-toluidine) (POT) remains largely unexplored in ternary systems. Because POT is a methyl-substituted derivative of PANI, its structural particularities are expected to influence both the electronic properties and interfacial interactions within the composite.

(ii) In contrast to the commonly reported methods involving hydrothermal synthesis, followed by *in situ* oxidative polymerization, the composites in this work are prepared *via* solid-state interactions. This approach avoids the use of oxidizing agents

and may lead to distinct interfacial organization and interaction mechanisms.

(iii) While most previous reports primarily focus on electrochemical applications (*e.g.*, supercapacitors, batteries, and sensors), the present study is centered on a detailed investigation of the physicochemical interactions between MoS_2, RGO, and POT. This is achieved through a correlated analysis using XRD, Raman, FTIR, and UV-Vis spectroscopies.

(iv) Additional insights are provided by studying the behavior of these composites in polar and nonpolar solvents, as well as under halogen light irradiation. The use of SERS to identify photochemical reaction products further distinguishes this work from previously reported studies.

2. Experimental

The following compounds were purchased from Merck company: molybdenum disulfide (MoS_2), reduced graphene oxide (RGO), *o*-toluidine (≥99%, OT), *N*-methyl-2-pyrrolidone (NMP), *N*,*N*′-dimethylformamide (DMF), acetone, toluene, potassium dichromate ($K_2Cr_2O_7$), sulfuric acid (H_2SO_4, 95.0–98.0%), acetonitrile (CH_3CN, ≥99.5%), Au nanoparticles with an average size of 10 nm and an ammonia solution (NH_4OH, 28–30%).

To prepare the composites, MoS_2 layers were prepared by mechanical exfoliation using the ball milling method, with 1 g of MoS_2 particles placed in a PM 100-RETSCH ball mill and ground at 600 rpm for 1 hour. This exfoliation technique provides a high yield and has economic sustainability, while the structural defects produced on the layer surfaces/edges are beneficial in various applications such as energy storage.[24]

POT-ES was prepared by the *in situ* chemical polymerization of OT, according to ref. 3. As reported in our previous study, the interaction of POT-ES with NH_4OH afforded POT-EB.[3] Four other samples were prepared, starting from a mixture of the three constituents, *i.e.*, MoS_2, POT-EB/POT-ES, and RGO. The concentrations of the three compounds in the four samples were as follows: (i) 50 wt%, 25 wt%, and 25 wt%, labelled as MoS_2/POT-EB/RGO 50 : 25 : 25; (ii) 50 wt%, 40 wt%, and 10 wt%, labelled as MoS_2/POT-EB/RGO 50 : 40 : 10; (iii) 50 wt%, 25 wt%, and 25 wt%, labelled as MoS_2/POT-ES/RGO 50 : 25 : 25; and (iv) 50 wt%, 40 wt%, and 10 wt%, labelled as MoS_2/POT-ES/RGO 50 : 40 : 10, respectively. The solid-state interaction of each reaction mixture took place by grinding for 30 min. Using the same protocol, the following binary composites were prepared: RGO/MoS_2, POT-EB/MoS_2, and POT-ES/MoS_2 with a MoS_2 concentration of 25 wt%.

The characterization of the MoS_2/POT-EB/RGO and MoS_2/POT-ES/RGO composites was performed by X-ray diffraction (XRD), Raman scattering, FTIR spectroscopy, and UV-Vis spectroscopy.

The XRD patterns of MoS_2/POT-ES/RGO composites were recorded using a Bruker D8 Advance X-ray diffractometer.

The Raman spectra of the MoS_2/POT-EB/RGO and MoS_2/POT-ES/RGO composites were recorded at an excitation wavelength of 1064 nm using a Bruker FT Raman spectrophotometer (model: MultiRAM).

The FTIR spectra of the MoS_2/POT-EB/RGO and MoS_2/POT-ES/RGO composites were recorded using a Bruker Vertex 80 FTIR spectrophotometer.

The UV-Vis spectra of MoS_2/POT-EB/RGO and MoS_2/POT-ES/RGO composites were recorded using a UV-Vis-NIR spectrophotometer (Lambda 950, PerkinElmer).

To study the photochemical processes of the MoS_2/POT-EB/RGO and MoS_2/POT-ES/RGO composites, a halogen lamp with a power of 100 W was used. The distance between the halogen lamp and the quartz cuvettes containing the solutions of the MoS_2/POT-EB/RGO and MoS_2/POT-ES/RGO composites in NMP, with a concentration of 0.2 mg mL^{-1}, was 10 cm. The products of photochemical reactions were studied by surface-enhanced Raman scattering (SERS) using Au nanoparticles as plasmonic substrates.

X-ray photoelectron spectroscopy (XPS) of the polymers POT-EB and POT-ES, as well as the MoS_2/POT-EB/RGO and MoS_2/POT-ES/RGO composites, was performed using a SPECS spectrometer equipped with a Phoibos 150 electron energy analyzer and a monochromatic X-ray source consisting of an aluminum anode (Al Kα 1486.74 eV).

The scanning electron microscopy (SEM) images of the MoS_2/POT-EB/RGO and MoS_2/POT-ES/RGO composites were recorded with a Zeiss Gemini 500 field-emission scanning electron microscope.

3. Results and discussion

3.1 Structural and vibrational properties of the composites based on MoS_2, POT, and RGO

Fig. 1 shows the XRD patterns of MoS_2 and the MoS_2/POT-ES/RGO 50 : 40 : 10 and MoS_2/POT-ES/RGO 50 : 25 : 25 composites.

In Fig. 1, it can be observed that all XRD patterns are characterized by an intense maximum located at $2\theta = 14.6°$, which is assigned to the (002) crystal plane. This maximum is accompanied by other lower-intensity maxima located at 2θ = 29.1°, 32.8°, 33.6°, 35.9°, 39.7°, 44.3°, 49.9°, 56°, 58.4°, 60.5°, 70.3°, 72.8°, 76°, 78.2°, 80.3°, and 88.7°, which are assigned to the crystalline planes (004), (100), (101), (102), (103), (006), (105),

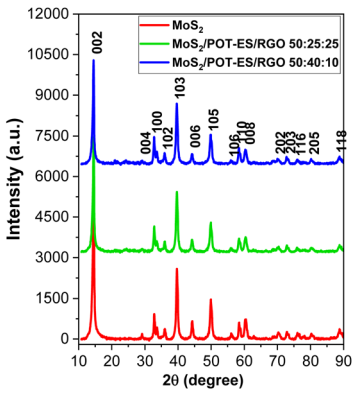

Fig. 1 XRD patterns of MoS_2 (red curve) and the MoS_2/POT-ES/RGO 50 : 25 : 25 (green curve) and MoS_2/POT-ES/RGO 50 : 40 : 10 (blue curve) composites.

(106), (110), (008), (202), (203), (116), (204), (205) and (118) of the 2H phase of MoS_2, respectively [PDF no. 04-003-3080]. Because the (002) crystal plane corresponds to the basal planes, *i.e.*, the superimposed S–Mo–S layers, and the (103) crystal plane corresponds to the nonbasal planes, which reflect the crystalline order in a different direction than that of the two-dimensional layer structure, a change in the intensity ratios of the peaks assigned to the crystalline planes (002) and (103) occurs from 2.84 to 1.93 and 1.74 in the case of MoS_2 and the composites MoS_2/POT-ES/RGO 50 : 25 : 25 and MoS_2/POT-ES/RGO 50 : 40 : 10, respectively. This experimental result can be because (a) the mass ratio of MoS_2 is diluted by 50% in the POT-ES- and RGO-containing compositions, according to the compositional ratios. As such, the drop in the intensities corresponding to the (002) planes to about 50% in the latter two compositions compared to the pure MoS_2 is understandable considering the large difference in the electron density (Z number) of the compared compositions. (b) The change in the intensity ratios of the above-mentioned (002) and (103) planes suggests that the shape or the aspect ratio of the nanocomposite's crystallites changes as well during this compositional dilution, most probably due to the presence of more and more POT-ES. The contribution of RGO in this sense appears not to be detectable. One may notice similar relative intensity changes for the peaks of other planes as well, sustaining the shape change of the crystallites in the composites. (c) Possible defects appear during the preparation.

Fig. 2 shows the SEM images of the MoS_2/POT-EB/RGO and MoS_2/POT-ES/RGO composites. Fig. 2a shows the large, crumpled RGO sheets, MoS_2 platelets with diameters ranging between 134 and 687 nm, and POT-EB particles with diameters between 24 and 39 nm, which mostly appear in an agglomerated form. Fig. 2b shows large, crumpled RGO sheets, MoS_2 platelets with diameters ranging between 121 and 377 nm, and isolated POT-ES particles with diameters between 21.2 and 38.2 nm. The MoS_2 platelets show a diameter between 115 nm and 1.088 μm (Fig. 2c).

An explanation for the small size of MoS_2 sheets in the composites with POT-EB/POT-ES and RGO must consider the synergy between the mechanical fragmentation induced by the grinding process and the exfoliation assisted by solid–solid interactions with the macromolecular compounds and RGO. The macromolecular chains of POT-EB/POT-ES reduce the cohesion of the MoS_2 interlayers, while the RGO layers stabilize the exfoliated fragments, preventing their reagglomeration. A consequence of these two effects is that, in the composites, MoS_2 flakes are significantly smaller than the starting material. As observed in Fig. 2d, the RGO layers are crumpled.

To understand the potential interactions between the three constituents, Fig. 3 and 4 show the Raman and FTIR spectra, respectively, of the MoS_2/POT-ES/RGO and MoS_2/POT-EB/RGO composites.

Fig. 3a shows the Raman lines of POT-EB peaked at 447, 1117, 1163, 1219, 1254, 1367, 1506 and 1618 cm^{-1}, which are assigned to the vibrational modes of deformation of the aromatic ring, deformation of the benzene ring (B) + C–H

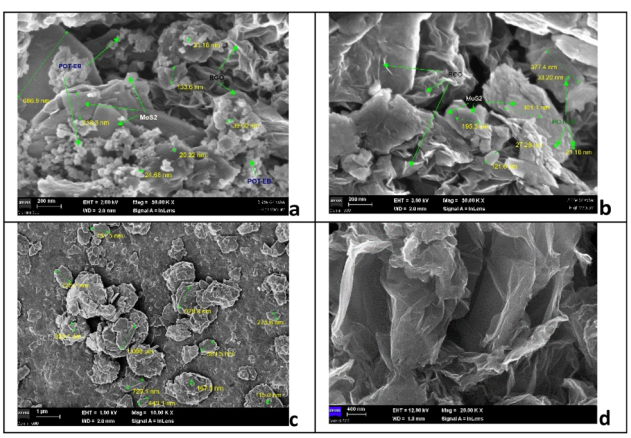

Fig. 2 SEM images of the MoS_2/POT-EB/RGO (a) and MoS_2/POT-ES/RGO (b) composites, MoS_2 (c) and RGO sheets (d).

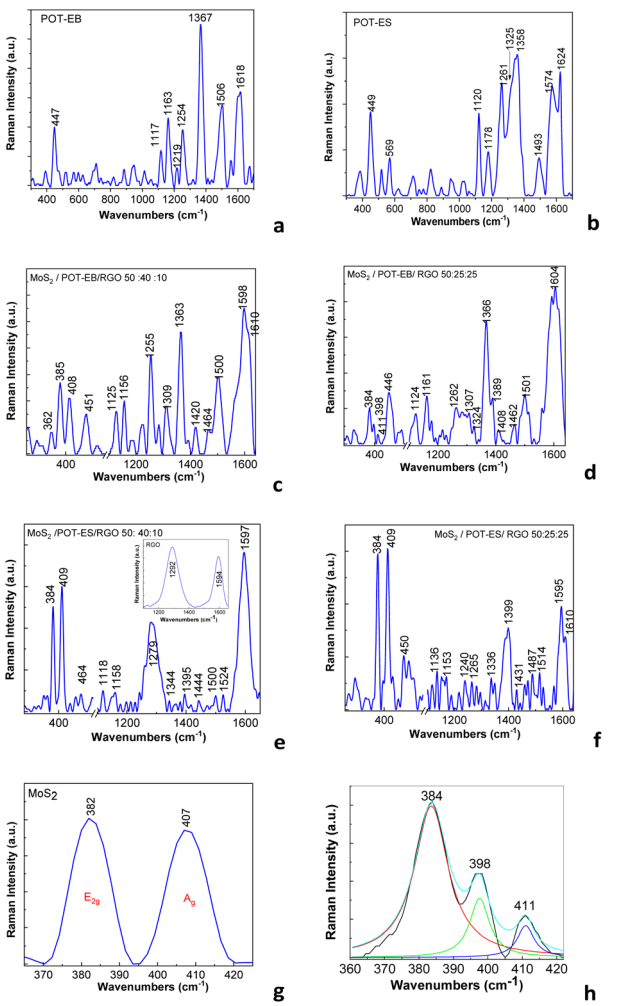

Fig. 3 Raman spectra of the POT-EB (a), POT-ES (b), MoS_2/POT-EB/RGO 50 : 40 : 10 (c), MoS_2/POT-EB/RGO 50 : 25 : 25 (d), MoS_2/POT-ES/RGO 50 : 40 : 10 (e), and MoS_2/POT-ES/RGO 50 : 25 : 25 (f) composites, and MoS_2 (g). Deconvolution of the Raman spectrum of MoS_2/POT-EB/RGO 50 : 25 : 25 (h). Inset of (e): Raman spectrum of RGO.

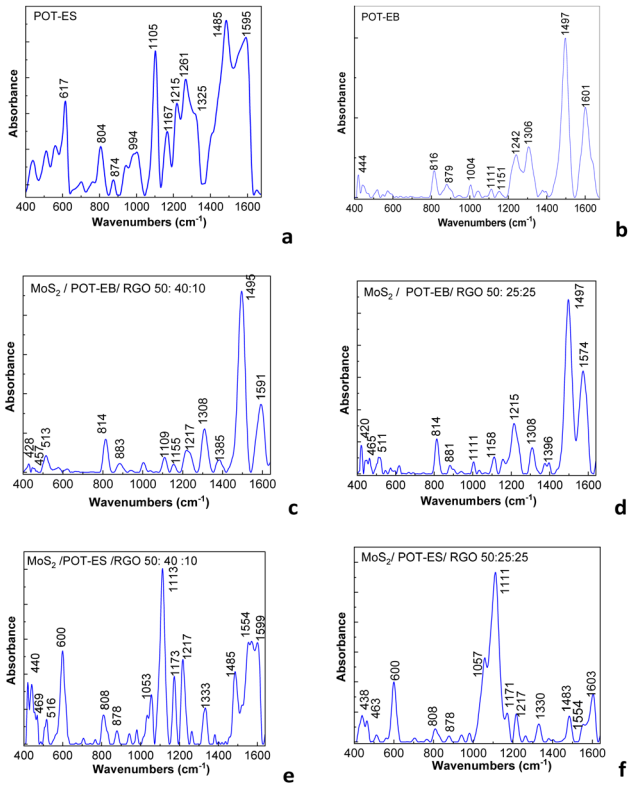

Fig. 4 FTIR spectra of POT-ES (a), POT-EB (b), MoS_2/POT-EB/RGO 50 : 40 : 10 (c), MoS_2/POT-EB/RGO 50 : 25 : 25 (d), MoS_2/POT-ES/RGO 50 : 40 : 10 (e), and MoS_2/POT-ES/RGO 50 : 40 : 10 (f).

bending in the CH_3 group, C–H bending in the B ring, C–N stretching + C–C stretching + C–H bending in the B ring, C–C stretching in the B ring, C–C stretching in the quinoid (Q) ring + C–H bending in the B ring, C=N stretching and C–C stretching + C–H bending in the B ring, respectively.[1,25] Fig. 3b shows the Raman lines of POT-ES located at 1178, 1261, 1325–1358, 1493, 1574, and 1624 cm^{-1}, which are assigned to the vibrational modes of C–H in-plane deformation, C–N bond stretching in the Q ring, C–N bond stretching in B–NH^+=Q, C–C + C–H + N–H bond stretching, the N=Q=N structure, and C–C + C–H bond stretching, respectively.[26] In the Raman spectra of the composites MoS_2/POT-EB/RGO 50 : 40 : 10 and MoS_2/POT-EB/RGO 50 : 25 : 25, the following lines can be observed: (a) the Raman lines situated at 1363–1366, 1500–1501, and 1598–1604 cm^{-1} belong to POT-EB and (b) the Raman lines at 384–385 and 408–411 cm^{-1} are assigned to the E_{2g} and A_g vibrational modes of MoS_2, respectively, which belong to the in-plane vibrations of the two sulfur atoms and the out-of-plane vibrations of the S atoms in the opposite directions, respectively.[27] The ratios between the intensities of the two Raman lines at 384–385 and 408–411 cm^{-1} ($I_{384–385}/I_{408–411}$) in the cases of the MoS_2/POT-EB/RGO 50 : 40 : 10 and MoS_2/POT-EB/RGO 50 : 25 : 25 composites are equal to 3.73 (Fig. 3c) and 1.28 (Fig. 3d), respectively, indicating an exfoliation process that weakens the interlayer interactions of MoS_2. An important role in the exfoliation process of MoS_2 is played by POT-EB, an assumption supported by the value of the $I_{383–385}/I_{408–410}$ ratio, which, in the case of the POT-EB/MoS_2 composite, is equal to 1.125 (Fig. S1b). For POT-EB-based composites, the $I_{E_{2g}}/I_{A_g}$ ratio increases compared to that of MoS_2, which is equal to 0.97 (Fig. 3e). This behavior may suggest a change in interlayer interactions. However, this change cannot be attributed exclusively to exfoliation. It may also reflect differences in the dispersion, local structure, or interaction with POT-EB and RGO. In the Raman spectra of the MoS_2/POT-ES/RGO 50 : 40 : 10 and MoS_2/POT-ES/RGO 50 : 25 : 25 composites, the POT-ES Raman lines are located at 1279–1265, 1343/1336–1395/1399, 1500–1493, 1597–1595 and 1624 cm^{-1} (ref. 26) and the MoS_2 Raman lines are located at 384 and 409 cm^{-1}.[3] The ratios between the intensities of the Raman lines peaked at 384 and 409 cm^{-1} in the case of MoS_2/POT-ES/RGO composites are equal to 0.97 (Fig. 3e) and 0.84 (Fig. 3f), lower than those reported for MoS_2 particles (Fig. 3g) or those of POT-ES/MoS_2 and RGO/MoS_2 composites, which show ratios equal to 1.64 (Fig. S1c) and 1.71 (Fig. S1a), respectively. This decrease can be associated with the weakening of the interlayer coupling. This effect is often correlated with exfoliation or increased disorder in the MoS_2 layers. However, the opposite trends observed for the POT-EB and POT-ES systems indicate that the intensity ratio alone cannot be used as a direct or universal measure of the degree of exfoliation in these composites. The Raman response is likely influenced by several factors, including charge transfer, defect density, and polymer–MoS_2 interactions. In addition, because the composites were prepared by solid-state milling, the extent of exfoliation is expected to be limited. Therefore, the observed spectral changes are more reasonably attributed to structural disorder and interfacial interactions than to a well-defined exfoliation process. However, this change cannot be attributed solely to exfoliation. This may also reflect differences in dispersion, local structure, or interaction with POT-EB and RGO.

Unlike the Raman spectrum of graphene recorded at an excitation wavelength of 532 nm (2.33 eV), in which the D band maximum is located at 1350 cm^{-1},[28] the Raman spectrum of RGO recorded at an excitation wavelength of 1064 nm (1.16 eV) shows the D band maximum located at 1290 cm^{-1}. This result is in good agreement with a previous study on the dependence of the D band on the excitation wavelength[29] and with the Raman studies reported at an excitation wavelength of 1064 nm.[30] Because the D and G bands of RGO are located at 1290 and 1598 cm^{-1}, associated with the defects visualized by the presence of carbon atoms with sp^3 hybridization and carbon atoms with sp^2 hybridization, respectively,[31] and POT-ES presents a Raman line at 1261 cm^{-1}, in the cases of the two MoS_2/POT-ES/RGO composites, it is observed that the D band of RGO is positioned at 1265 cm^{-1} (Fig. 3f) and 1279 cm^{-1} (Fig. 3e), which indicates a tension in the basal plane of RGO due to adsorption on the more rigid structure of the polymer generated by its interaction with MoS_2. Other changes observed in Fig. 3 concern the shift of the Raman line from 1178 cm^{-1} for PANI-ES (Fig. 3f) to 1158 cm^{-1} (Fig. 3d) and 1153 cm^{-1} (Fig. 3b). This result indicates a change in the component of the structural units from the emeraldine to leucoemeraldine type, with the latter presenting a line at 1157 cm^{-1} in the Raman spectrum, associated with the C–H vibrational mode.[32]

In order to explain these variations, Fig. 4 highlights the FTIR spectra of MoS_2/POT-EB/RGO and MoS_2/POT-ES/RGO. As shown in Fig. 4, the FTIR spectrum of POT-ES shows IR bands located at 994, 1105, 1167, 1261, 1325, 1485 and 1595 cm^{-1} (Fig. 4a), assigned to the vibrational modes of deformation of the benzene ring, deformation of the benzene ring + C–H, the C–H bond in the quinoid ring, stretching of the C–N bond in the B–NH^+═Q entity, stretching of the C–N bond in the vicinity of the quinoid ring, stretching of the C–C + C–H + N–H bonds, and the N–H bond in the N═Q═N structure, respectively.[25,33,34] The FTIR spectrum of POT-EB shows IR bands located at 1004, 1111, 1151, 1242, 1306, 1497 and 1601 cm^{-1} (Fig. 4b), assigned to the vibrational modes of deformation of the benzene ring (B), deformation of B + C–H, the C–H bond in the quinoid ring (Q), stretching of the C–N bond in the B–N═Q entity, stretching of the C–N bond in the vicinity of Q, stretching of the C–C + C–H + N–H bonds, and the N–H bond in the N═Q═N structure, respectively.[25,33] In the FTIR spectra of the MoS_2/POT-ES/RGO 50 : 40 : 10 and MoS_2/POT-ES/RGO 50 : 25 : 25 composites, the IR bands of POT are shifted from 617, 1105, 1325 and 1595 cm^{-1} (Fig. 4a) to 600, 1113–1111, 1333–1330 and 1599–1603 cm^{-1} (Fig. 4e and f), respectively, along with changes in their absorbance and the presence of a new IR band at 1053–1057 cm^{-1}, which belongs to the symmetric vibrational mode of the S–O bond in HSO_4^- ions.[35] According to the vibrational studies reported by S. Quillard *et al.*,[25] the polyaniline class compounds to which POT is related in the form of LB exhibit IR bands at *ca.* 1118 and 1603 cm^{-1}, which are assigned to the B_{2u} and B_{3g} vibrational modes, respectively, while the N–N′-diphenyl-1,4-phenylene diamine structural units in LB exhibit IR bands at 600 and 1331 cm^{-1}, and these bands are close to those present in the FTIR spectra of the MoS_2/POT-ES/RGO composites at 600, 1111–1113, 1330–1333 and 1603–1599 cm^{-1}. An interesting fact noted in Fig. S2b is that the IR bands assigned to the B_{2u} and B_{3g} vibrational modes are also observed in the IR spectrum of the composite, resulting from the interaction of POT-EB with MoS_2, and these are located at 1115 and 1601 cm^{-1}, respectively. A previous study reported by Z. Ping *et al.*[36] demonstrated that PANI in the form of LS exhibits IR bands at 1336 and 1606 cm^{-1}, which are also close to those observed for the MoS_2/POT-ES/RGO composites at 1330–1333 and 1603–1599 cm^{-1}, respectively. In the FTIR spectrum of the composite resulting from the interaction of POT-ES with MoS_2, it is observed that the two IR bands are located at 1338 and 1610 cm^{-1} (Fig. S2c). In the FTIR spectra of the MoS_2/POT-EB/RGO 50 : 40 : 10 and MoS_2/POT-EB/RGO 50 : 25 : 25 composites, the IR bands belonging to POT are observed, and the IR bands at 1242 and 1601 cm^{-1} (Fig. 4b) have shifted to 1217–1215 and 1591–1574 cm^{-1}, respectively (Fig. 4c and d). The presence of IR bands at 1591 and 1215 cm^{-1} indicates an interaction of the POT-EB interface with MoS_2 and RGO, leading to the partial transformation of POT-EB into POT-ES. Considering the changes illustrated by IR spectroscopy and Raman scattering, the solid-state reaction of POT-EB and POT-ES, respectively, with MoS_2 and RGO can take place according to Fig. 5.

In our opinion, Fig. 5 highlights that the reaction products of (a) POT-ES with MoS_2 and RGO correspond to a ternary composite (TC) of the type RGO non-covalently functionalized with pseudo-protonic POT doped with MoS_2 and a binary composite (BC) of the type RGO covalently functionalized with POT-LS, while those of (b) POT-EB with MoS_2 and RGO correspond to a TC of the type RGO non-covalently functionalized with pseudo-protonic POT doped with MoS_2 and a BC of the type RGO covalently functionalized with POT-LB.

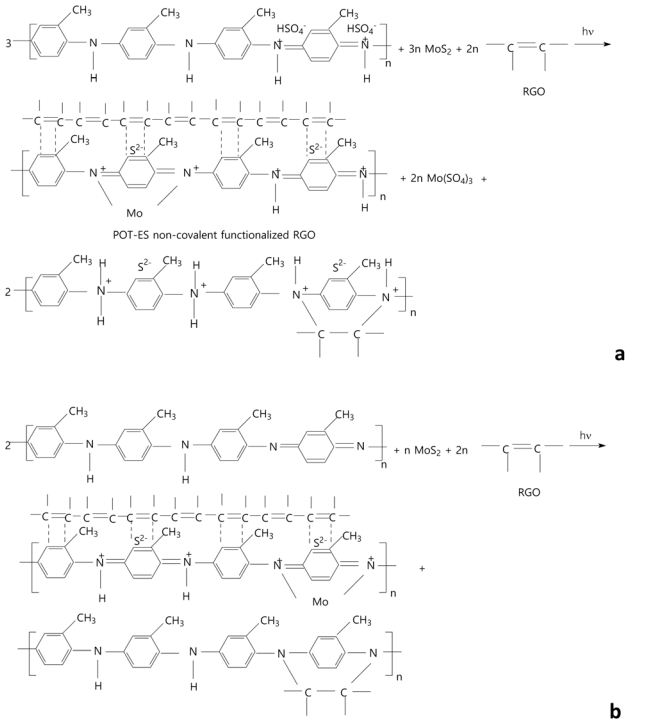

Fig. 5 Interactions of (a) POT-ES and (b) POT-EB with MoS_2 and RGO.

A schematic representation of the reaction products presented above is illustrated in Fig. 6.

Fig. S2a shows the FTIR spectrum of MoS_2, which is characterized by an intense IR band at 469 cm^{-1}, assigned to the in-plane asymmetrical vibration of Mo and S atoms, with the A_{2u} symmetry.[37] This IR band, in the case of the composites MoS_2/POT-EB/RGO 50 : 40 : 10 (Fig. 4c), MoS_2/POT-ES/RGO 50 : 40 : 10 (Fig. 4d), MoS_2/POT-EB/RGO 50 : 25 : 25 (Fig. 4e), MoS_2/POT-ES/RGO 50 : 25 : 25 (Fig. 4f), POT-EB/MoS_2 (Fig. S2b), and POT-ES/MoS_2 (Fig. S2c), peaks at 469, 457, 463, 465, 469, and 469 cm^{-1}, respectively. The shift of the IR band maximum attributed to the vibrational modes of MoS_2, observed only in the ternary composites MoS_2/POT-EB/RGO and MoS_2/POT-ES/RGO, indicates a significant modification of the electronic and structural environment of MoS_2. The presence of RGO favors the formation of an electronic coupling network between MoS_2 and the POT chains (especially in the salt form), which leads to charge transfer and/or local strains on the Mo–S network. Other proofs that support Fig. 5 are provided in the following discussions using XPS studies. Fig. 7 presents the XPS spectra of the macromolecular compounds POT-EB and POT-ES, as well as the composites MoS_2/POT-EB/RGO 50 : 25 : 25 and MoS_2/POT-ES/RGO 50 : 25 : 25.

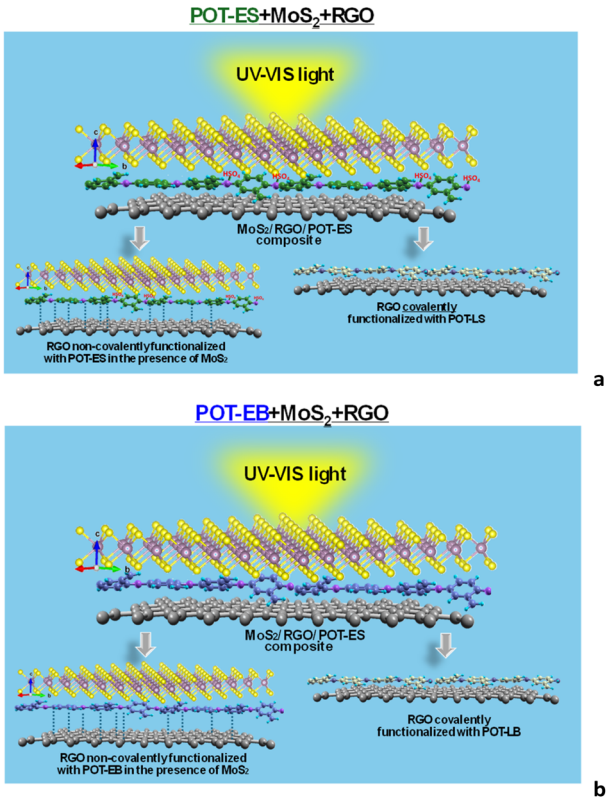

Fig. 6 Schematic of the products resulting from the interactions of (a) POT-ES and (b) POT-EB with MoS_2 and RGO.

Fig. 7a–d show the deconvolution of the C 1s and N 1s spectra of POT-EB and POT-ES. In the XPS C 1s spectrum of POT-EB, the four bands at 284.1, 284.7, 285.4, and 286.2 eV are assigned to the C═C, C–C/C–H, C–N/C═N, and C–O–H bonds, respectively,[38] while the bands in the deconvoluted XPS C 1s spectrum of POT-ES are situated at 284.2, 284.8, 285.6, and 287 eV, respectively. The change in the ratio between the area of the peaks assigned to the C═C and C–C/C–H bonds from 0.82 to 1.73 is a consequence of the protonated structure of POT-ES. In the XPS N 1s spectrum of POT-EB, the two high-intensity bands at 398.4 and 399.4 eV are attributed to the imine (C═N–C) and amine (C–NH–C) bonds, accompanied by two low-intensity bands at 400.8 and 402.5 eV, assigned to protonated amine ($–NH_2^+$) and protonated imine (C–NH^+═C), respectively.[39] The deconvolution of the XPS N 1s spectrum of POT-ES shows three high-intensity bands at 399.4, 400.7, and 401.9 eV, accompanied by a low-intensity band at 403.7 eV.

Fig. 7f-n show the deconvolution of the C 1s, N 1s, Mo 3d and S 2p spectra of MoS_2/POT-EB/RGO 50 : 25 : 25 and MoS_2/POT-ES/RGO 50 : 25 : 25. In the XPS C 1s spectra of the MoS_2/POT-EB/RGO 50 : 25 : 25 and MoS_2/POT-ES/RGO 50 : 25 : 25 composites, there are five bands at 284.8, 284.2, 285.4–285.5, 286.5, and 288.6–288.1 eV, having ratios between the area of the peaks assigned to the C═C and C–C/C–H bonds equal to 0.04 and 0.44, respectively. This decrease is a consequence of the covalent functionalization of RGO with POT-LB (Fig. 5b) and POT-LS (Fig. 5a), respectively. In the XPS N 1s spectra of the MoS_2/POT-

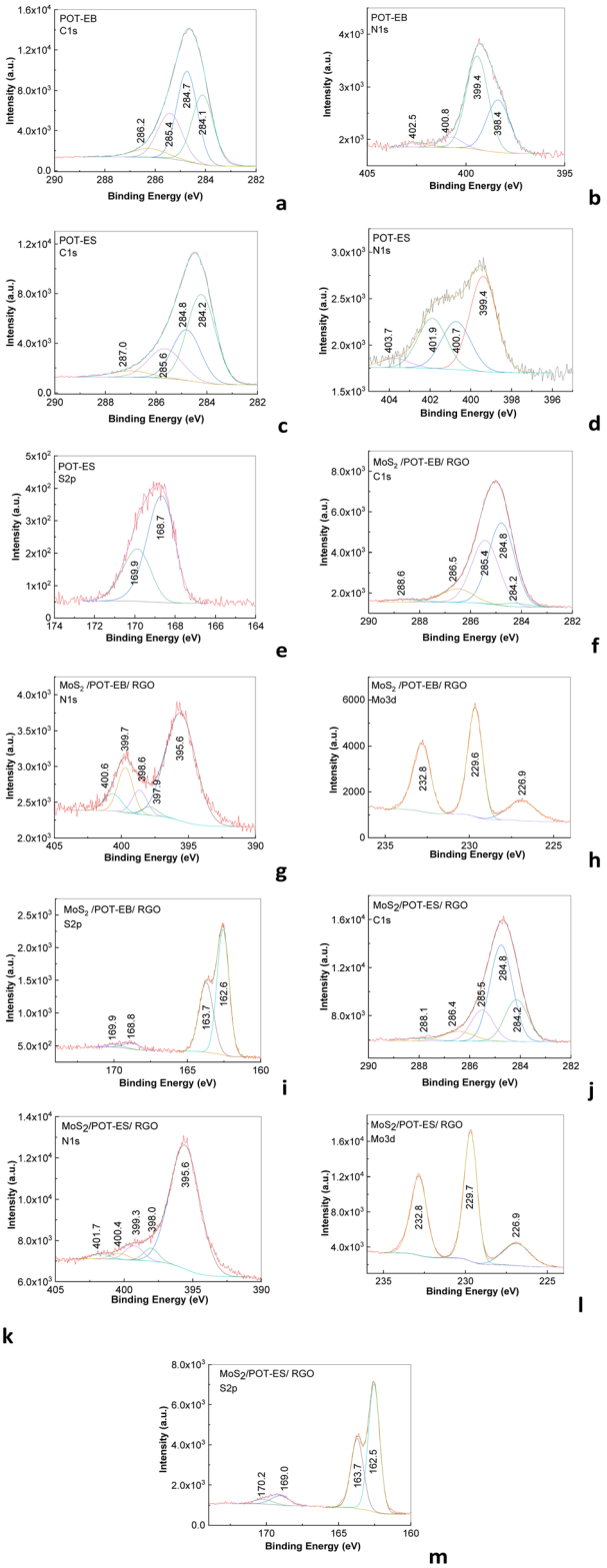

Fig. 7 XPS C 1s (a) and N 1s (b) spectra of POT-EB. XPS C 1s (c), N 1s (d) and S 2p (e) spectra of POT-ES. XPS C 1s (f), N 1s (g), Mo 3d (h) and S 2p (i) spectra of MoS_2/POT-EB/RGO 50 : 25 : 25. XPS C 1s (j), N 1s (k), Mo 3d (l) and S 2p (m) spectra of MoS_2/POT-ES/RGO 50 : 25 : 25.

EB/RGO 50 : 25 : 25 and MoS_2/POT-ES/RGO 50 : 25 : 25 composites, the five bands at 395.6, 397.9–398.0, 398.6–399.3, 399.7–400.4, and 400.6–401.7 eV are assigned to the C–N^+(R)=C (R= Mo, as Mo $3p_{3/2}$), C=N–C, C–NH–C, –NH_2^+– and C–NH^+=C bonds, respectively;[39] the presence of the band at 395.6 eV must to correlated to the reaction product of the type RGO non-covalently functionalized with pseudo-protonic POT doped with MoS_2, as shown in Fig. 5a and b. In the XPS Mo 3d spectra of the MoS_2/POT-EB/RGO 50 : 25 : 25 and MoS_2/POT-ES/RGO 50 : 25 : 25 composites, three bands at 226.9, 229.7 and 232.8 eV are observed, and they are assigned to S 2 s in sulfide, Mo $3d_{5/2}$ in sulphide (Mo^{4+}) and Mo $3d_{5/2}$ in sulphate or Mo^{6+} $3d_{5/2}$, respectively.[40,41] In the XPS S 2p spectra of the MoS_2/POT-EB/RGO 50 : 25 : 25 and MoS_2/POT-ES/RGO 50 : 25 : 25 composites as well as of POT-ES (Fig. 7e), the four bands peaked at 168.8–169, 169.9–170.2, 162.6–162.5 and 163.7 eV are assigned to the S $2p_{3/2}$ and S $2p_{1/2}$ of the S–O bond of molybdenum sulfate, S $2p_{3/2}$ of the Mo–S bond and S $2p_{3/2}$ of the S–C bond, respectively.[29,41]

3.2 Photochemical processes of the composites based on MoS_2, POT, and RGO

Fig. 8 shows the UV-Vis spectra of the solutions of MoS_2/POT-EB/RGO and MoS_2/POT-ES/RGO, both in NMP, having a concentration of 0.2 mg mL^{-1}, and their evolution under exposure to light emitted by a halogen lamp.

In the initial state, the UV-Vis spectra of the MoS_2/POT-EB/RGO 50 : 40 : 10 and MoS_2/POT-ES/RGO 50 : 40 : 10 composites (Fig. 8a and b) show a band with high absorbance located in the spectral range of 250–400 nm and another with lower absorbance having a maximum at ~558 and 578 nm, respectively. The analysis of Fig. 8c and d indicates that these bands belong to POT-EB and POT-ES, respectively, and the UV-Vis spectra is characterized in the initial state by a band with high absorbance located in the spectral range of 250–400 nm and another with lower absorbance having a maximum located at 604 and 614 nm, which, by comparison with PANI, is assigned to the π–π* transition in B, and the second one is attributed to the π–π* transition in the Q structure of POT-EB and the polaronic structure in POT-ES.[42,43] The shift of the bands from 604 nm (Fig. 8c) and 614 nm (Fig. 8d) to 558 nm (Fig. 8a) and 578 nm (Fig. 8b) is due to the interaction of POT-EB and POT-ES with MoS_2 and RGO, respectively. These shifts must consider the pseudo-protonic doping of POT in the presence of MoS_2, which changes the effective conjugation length as well as the charge transfer between POT and RGO, leading to the covalent functionalization of RGO with POT. A similar behavior is reported in the case of the MoS_2/POT-ES/RGO 50 : 25 : 25 composite (Fig. 8e). A careful analysis of Fig. 8 indicates that in the UV-Vis spectra of the MoS_2/POT/RGO composites, the characteristic POT bands are predominantly observed, while the excitonic bands of MoS_2 are no longer visible. This is due to their overlapping and masking by the intense absorptions of the polymer, the charge transfer between MoS_2-POT/RGO, and the fragmentation of the MoS_2 layers, which leads to the suppression of the individual optical signature of MoS_2 in the composite. A similar

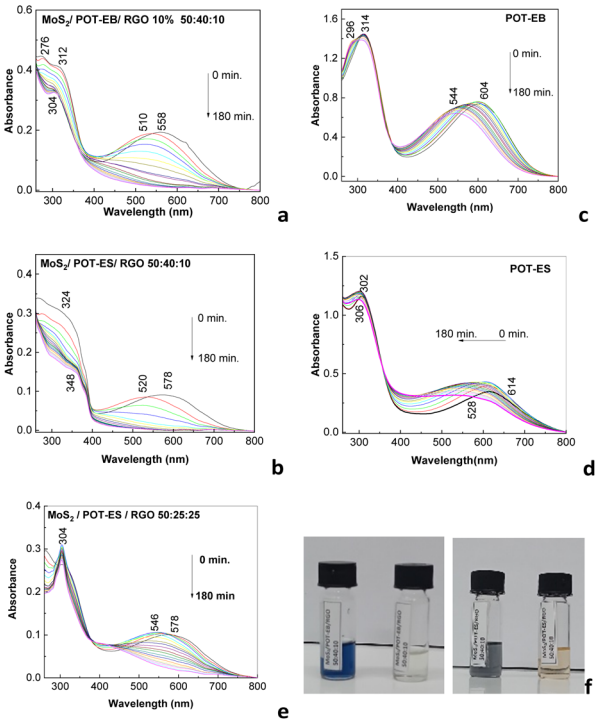

Fig. 8 UV-Vis spectra of the MoS_2/POT-EB/RGO 50 : 40 : 10 (a) and MoS_2/POT-ES/RGO 50 : 40 : 10 (b) composites, conjugated polymers POT-EB (c) and POT-ES (d), and MoS_2/POT-ES/RGO 50 : 25 : 25 (e) in NMP and their evolution with exposure to the light emitted by a halogen lamp for 180 min. (f) Color changes of the MoS_2/POT-EB/RGO 50 : 40 : 10 and MoS_2/POT-ES/RGO 50 : 40 : 10 composites before and after exposure to the light emitted by a halogen lamp for 180 min. In (a–e), the colors black, red, green, blue, cyan, yellow, dark yellow, navy, purple, wine, olive, dark cyan, royal, orange, light yellow, gray, light magenta, light cyan and pink correspond to 0, 10, 20, 30, 40, 50, 60, 70, 80, 90, 100, 110, 120, 130, 140, 150, 160, 170 and 180 min, respectively, of exposing the samples to the light emitted by the halogen lamp.

behavior is observed in the case of the binary POT/MoS_2 composites (Fig. S3a and b). The exposure of the MoS_2/POT-EB/RGO 50 : 40 : 10 and MoS_2/POT-ES/RGO 50 : 40 : 10 composites to UV light induces, in the first 40 minutes, a shift of the bands from 558 nm and 578 nm to 510 nm and 520 nm, respectively. This shift can be explained by taking into account the hydrogen bonds[43] established between the C=O group of NMP and the N–H bonds of POT-EB/POT-ES, as well as the orientation of the dipoles of NMP *vs.* the positive charges of POT-ES or the lone pair of amine groups of POT-EB, which induce changes in the orientation of macromolecular chains.[44] In the next 140 minutes, the above-given change is followed by a gradual decrease in the absorbance of these bands until their disappearance. The same is not observed in the cases of POT-EB and POT-ES. In these two cases, a shift of the maximum from 604 and 614 nm to 544 and 528 nm, respectively, is observed during 180 min of UV irradiation, with a slight change in the absorbance of this band. This shift can be explained by considering Fig. 5, in which it is observed that compared with PANI-EB and PANI-ES, a decrease in the conjugation degree of

macromolecular compounds occurs as a consequence of the charge transfer induced by 2D materials and the torsion of the rings by the covalent coordinative binding of Mo to the imine groups of the quinoid rings of POT.

To verify whether the above-mentioned changes in the electronic transitions are related to the polar or non-polar character of the solvent used, Fig. 9 shows the evolution of the UV-Vis spectra of the MoS_2/POT-EB/RGO 50 : 40 : 10 composite in toluene and acetone when the two solutions are exposed to light emitted by the halogen lamp.

The analysis of Fig. 9 highlights that the UV-Vis spectra of the MoS_2/POT-EB/RGO composite in toluene and acetone are characterized by a band with high absorbance having a maximum at 310 nm and another located in the spectral range of 400–800 nm with maxima at 554 nm (Fig. 9a) and 570 nm (Fig. 9b). Exposure of the MoS_2/POT-EB/RGO 50 : 40 : 10 composite in toluene to light emitted by a halogen lamp does not induce significant variations in the position of the band at 554 nm (Fig. 9a), while in the case of the MoS_2/POT-EB/RGO 50 : 40 : 10 composite in acetone, it induces a shift of the band from 570 nm to 520 nm (Fig. 9b), without significant variations in the absorbance.

At this stage of our studies, a question remains: what happens when the MoS_2/POT-EB/RGO composite in NMP is exposed to light emitted by the halogen lamp? At present, we are tempted to put forward two hypotheses. The first one is the degradation of the macromolecular chain until very short fragments are obtained, and some of them are similar to the *o*-toluidine monomer, while the second hypothesis takes into account the generation of POT-LS. The blue curve in Fig. 10a shows that the *o*-toluidine band in the UV-Vis spectrum is located at 294 nm, which indicates that the degradation of the macromolecular chain to entities similar to the monomer does not take place. To verify the second hypothesis, the solutions of POT-EB and POT-ES, both dissolved in NMP, were interacted with the hydrazine solution. One observes that, as shown in Fig. 10a and b, the UV-Vis spectra are characterized only by a band having a maximum at 318 and 320 nm, respectively, very close to that of the two polymers.

The band in the 400–800 nm range in the case of POT-EB/POT-ES does not disappear due to the lack of a source of excited carriers of MoS_2 and a fast electron transporter such as RGO. A significant factor in the appearance of POT-ES is the photodegradation of NMP.[45] In this context, the second hypothesis should take into account the fact that NMP under

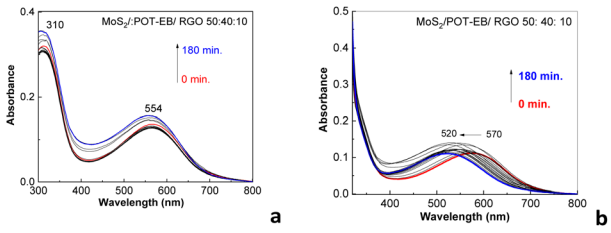

Fig. 9 UV-Vis spectra of the MoS_2/POT-EB/RGO 50 : 40 : 10 composite in toluene (a) and acetone (b).

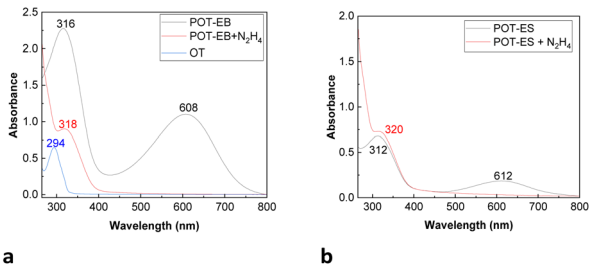

Fig. 10 UV-Vis spectra of (a) OT and POT-EB and (b) POT-ES in NMP before and after interaction with hydrazine.

light emitted by a halogen lamp can be degraded by breaking the –C–C–C=O and N–CH_3 bonds, with the formation of $^{\bullet}$C=O, $^{\bullet}$C–C=O, $C_4H_3ON^{\bullet}$, and $CH_3^{\bullet}$ radicals, which can interact with the RGO sheets, leading to the transformation of RGO non-covalently functionalized with pseudo-protonic POT doped with MoS_2 into RGO and POT-ES. A recent study demonstrated that NMP improves H_2S absorption performance and reduces the energy required for solvent regeneration compared to amine-only solutions.[46] Considering this reference and focusing on the products of the reaction shown in Fig. 5a, the following photochemical reactions can be envisaged to occur in the case of pseudo-protonic POT in the presence of MoS_2 and POT-LS covalently functionalized RGO in the presence of NMP (Fig. 11).

A schematic presentation of the photochemical reaction products of pseudo-protonic POT doped with MoS_2 and POT-LS covalently functionalized RGO is shown in Fig. 12.

In this stage of our study, we are tempted to attribute the variations observed in Fig. 8 to the transformation of the RGO sheets non-covalently functionalized with pseudo-protonic POT doped with MoS_2 and POT-LS covalently functionalized RGO into RGO sheets modified with radicals of NMP, pseudo-protonic POT doped with MoS_2 and POT-LB covalently functionalized RGO, respectively. Additional information is shown in Fig. 13, which

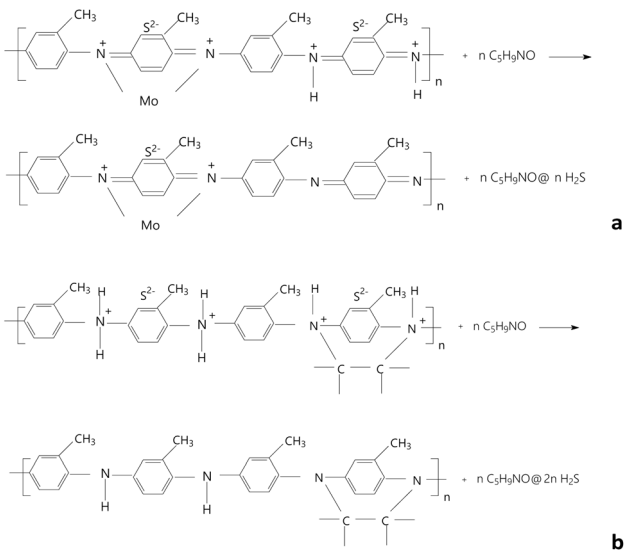

Fig. 11 Photochemical reaction of pseudo-protonic POT doped with MoS_2 and POT-LS covalently functionalized RGO.

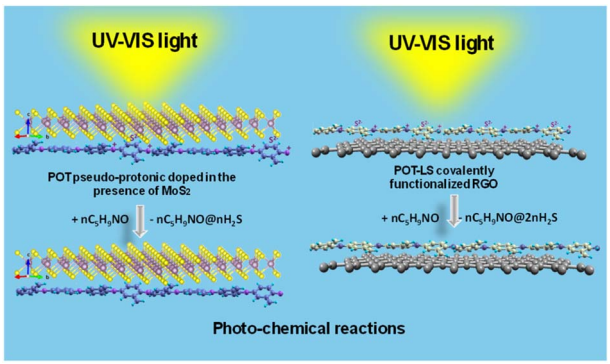

Fig. 12 Schematic of the photochemical reaction products of pseudo-protonic POT doped with MoS_2 and POT-LS covalently functionalized RGO.

shows the SERS spectra of the MoS_2/POT-ES/RGO 50 : 40 : 10 composite after irradiation for 180 min in the presence of Au nanoparticles with an average size of 10 nm. According to Fig. 13a, when 40 μL of MoS_2/POT-ES/RGO 50 : 40 : 10 in NMP with a concentration of 0.2 mg mL^{-1} is added to 1 mL of Au nanoparticles, the SERS spectra show Raman lines belonging to (a) MoS_2 located at 374 and 407 cm^{-1} and (b) POT having maxima at 623, 754, 860, 933, 1030, 1120, 1155–1173, 1228, 1309, 1370, 1431, 1458-1479-1510, and 1583 cm^{-1}, belonging to the vibrational modes of the benzene ring deformation in LB-type structural units, *N*,*N*′-diphenyl-1 entities, 4-phenylenediamine (PCD) entities, C–H bending in the benzene ring, cation radical entities, benzene ring deformation, benzene ring deformation + C–H bending, C–H bending, C–N stretching, PCD entities, protonated or pseudo-protonated structures (–NX^+–, where X is H, Mo), C–C stretching + C–H stretching, and C=C stretching in the benzene ring, respectively.[25,26,32,34] In our opinion, the presence of these Raman lines, peaked at 623, 754, 860, 933, 1120, 1155–1173, 1228, 1309, 1431, 1458–1479–1510, and 1583 cm^{-1}, confirms the structure of LB of POT covalently functionalized RGO, while the Raman line peaked at 1370 cm^{-1}, which is situated in the vicinity of the Raman lines of POT-ES (1358 cm^{-1}, Fig. 3f) and its composites with MoS_2 and RGO (1336–1399 cm^{-1}, Fig. 3b), confirms the structure of the pseudo-protonic doped state of POT.

The subsequent interaction of the MoS_2/POT-ES/RGO 50 : 40 : 10 composite solution after 180 min of exposure to light emitted by a halogen lamp with a 0.5H_2SO_4 solution leads to (i) the shift of the Raman line from 1173 and 1309 cm^{-1} (Fig. 13a) to 1195 and 1292 cm^{-1}, respectively (Fig. 13b); (ii) the shift of the Raman line from 1370 cm^{-1} (Fig. 13a) to 1378 cm^{-1} (Fig. 13b), along with an increase in intensity; (iii) the modification of the ratio between the intensities of the Raman lines located in the spectral range of 1400–1500 cm^{-1} (Fig. 13b); and (iv) the shift of the Raman line from 1583 cm^{-1} (Fig. 13a) to 1558 cm^{-1} (Fig. 13b). These variations originate from the protonation of the reaction products shown in Fig. 11, with their transformation into POT-LS, according to Fig. 14.

In our opinion, Fig. 12 proves the protonic acid doping of the reaction products of the MoS_2/POT-EB/RGO composite in NMP after exposure to light emitted by a halogen lamp for 180 min, which, in Fig. 13b, is marked by the Raman line peaked at 1378 cm^{-1}.

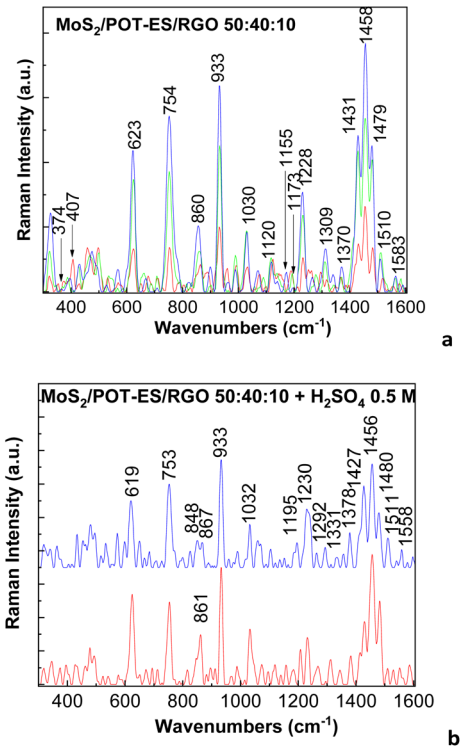

Fig. 13 SERS spectra of the MoS_2/POT-ES/RGO 50 : 40 : 10 composite after 180 min of exposure to light emitted by a halogen lamp. The red, green, and blue curves correspond to 40, 120, and 180 μL of the MoS_2/POT-ES/RGO composite in 1 mL of Au nanoparticles with an average size of 10 nm, respectively (a). Interaction of 180 μL of the MoS_2/POT-ES/RGO 50 : 40 : 10 composite with 120 μL (red curve) and 180 μL (blue curve) of 0.5 M H_2SO_4 (b).

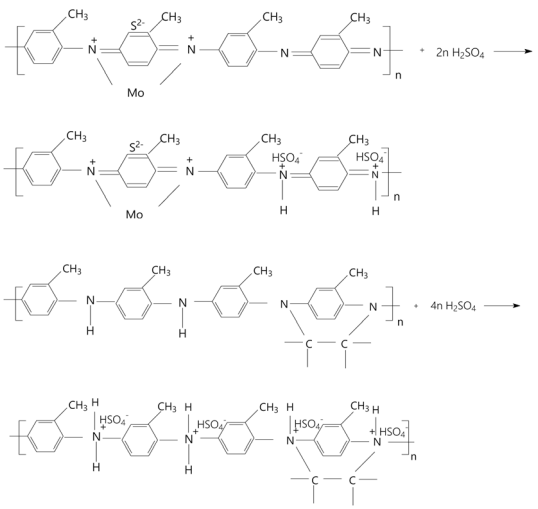

Fig. 14 Interaction of H_2SO_4 with the reaction products of the MoS_2/POT-EB/RGO composite in NMP after exposure to the light emitted by a halogen lamp for 180 min.

4. Conclusions

This work reports new results concerning the synthesis and optical properties of composites based on MoS_2, POT, and RGO. Binary and ternary composites were prepared. They were obtained through solid-state interactions between MoS_2, RGO sheets, and POT-EB/POT-ES. The conclusions obtained are as follows:

(i) Changes in Raman and FTIR spectra indicate that the interaction of POT-ES with MoS_2 and RGO leads to a ternary composite of the type RGO non-covalently functionalized with pseudo-protonic POT doped with MoS_2 and a binary composite of the type RGO covalently functionalized with POT-LS. The interaction of POT-EB with MoS_2 and RGO leads to a ternary composite of the type RGO non-covalently functionalized with pseudo-protonic POT doped with MoS_2 and a binary composite RGO covalently functionalized with POT-LS. The formation of these composites involves the generation of additional defects in the MoS_2 sheets, according to XRD studies.

(ii) The UV-Vis spectra of the two macromolecular compounds, *i.e.*, POT-EB and POT-ES, are characterized by two bands. The first one is situated in the spectral range of 250–400 nm, and the second one has the maximum located at 604 and 614 nm, respectively, which are assigned to the π–π* transition in the benzene ring of POT-EB and the π–π* transition in the quinoid structure of the polaronic structure of POT-ES, respectively. In the case of the composites resulting from the solid-state interaction of MoS_2 with RGO sheets and POT-EB or POT-ES, the band assigned to the π–π* transition in the benzene ring is reported to have a maximum at 558 and 578 nm, respectively. These changes are caused by the pseudo-protonic doping of POT in the presence of MoS_2, which changes the effective conjugation length as well as the charge transfer between POT and RGO. As a result, the covalent functionalization of RGO with POT occurs.

(iii) The exposure of the mixture containing ternary and binary composites dissolved in NMP to light emitted by a halogen lamp leads to a transformation of the RGO sheets non-covalently functionalized with pseudo-protonic POT doped with MoS_2 and POT-LS covalently functionalized RGO into RGO sheets, pseudo-protonic POT doped with MoS_2, and POT-LB covalently functionalized RGO. UV-Vis spectroscopic studies highlight this photochemical interaction through the disappearance of the band situated in the spectral range of 400–800 nm and the presence of a band localized between 200 and 400 nm.

(iv) The interaction of H_2SO_4 with pseudo-protonic POT doped with MoS_2 and POT-LB covalently functionalized RGO leads to composites like those proposed in Fig. 14.

Author contributions

Madalina Cercel: visualization, methodology, investigation, formal analysis. Andreea Nila: visualization, methodology, investigation, formal analysis. Ion Smaranda: visualization, methodology, investigation, formal analysis. Andreea Androne: visualization, methodology, investigation, formal analysis. Teodora Burlanescu: visualization, methodology, investigation, formal analysis. Adam Lörinczi: visualization, methodology, investigation, formal analysis. Catalin Negrila: investigation, methodology, formal analysis. Elena Matei: investigation, methodology, formal analysis. Mihaela Baibarac: methodology, investigation, formal analysis, writing – original draft, writing – review and editing, validation, supervision, resources, project administration, conceptualization.

Conflicts of interest

The authors declare that they have no known competing financial interests or personal relationships that could have appeared to influence the work reported in this paper.

Data availability

The data that support the findings of this study are available from the corresponding author, Dr Mihaela Baibarac, upon reasonable request.

Supplementary information (SI) is available. See DOI: https://doi.org/10.1039/d5na01164g.

Acknowledgements

This work is funded by the Core Program of the National Institute of Materials Physics, granted by the Romanian Ministry of Research, Innovation, and Digitization, through the PC3-PN23080303.

References

1 K. Gopalakrishnan, A. Sultan, A. Govindaraj and C. N. R. Rao, Supercapacitors based on composites of PANI with nanosheets of nitrogen-doped RGO, BC1.5N, MoS_2, and WS_2, *Nano Energy*, 2015, **12**, 52–58.

2 F. Y. Xiong, Z. Y. Cai, L. B. Qu, F. P. Zhang, Z. F. Yuang, O. K. Asare, *et al.*, Three-dimensional crumpled reduced graphene oxide/MoS_2 nanoflowers: a stable anode for lithium-ion batteries, *ACS Appl. Mater. Interfaces*, 2015, **7**, 12625–12630.

3 T. Burlanescu, M. Cercel, I. Smaranda, A. Androne, I. Zgura, P. C. Ganea, C. Negrila, A. Lorinczi, C. Bartha and M. Baibarac, Optical, structural and electrical properties of composites based on MoS_2, WS_2 and poly(orto-toluidine), *Mater. Today Commun.*, 2025, **46**, 112469.

4 X. Li, C. F. Zhang, S. Xin, Z. C. Yang, Y. T. Li, S. W. Zhang and P. Yao, Facile synthesis of MoS_2/Reduced graphene oxide @ polyaniline for high-performance supercapacitors, *ACS Appl. Mater. Interfaces*, 2016, **8**, 21373–21380.

5 D. Xie, D. H. Wang, W. J. Tang, X. H. Xia, Y. L. Zhang, X. L. Wang, C. D. Gu and J. P. Tu, Binder-free network-enabled MoS_2-PPY-rGO ternary electrode for high capacity and excellent stability of lithium storage, *J. Power Sources*, 2016, **307**, 510–518.

6 W. W. Qin, Y. Li, Y. Q. Teng and T. Qin, Hydrogen bond-assisted synthesis of MoS_2/reduced graphene oxide

composite with excellent electrochemical performances for lithium and sodium storage, *J. Colloid Interface Sci.*, 2018, **512**, 826–833.

7 G. S. Geleta, Z. Zhao and Z. X. Wang, A novel reduced graphene oxide/molybdenum disulfide/polyaniline nanocomposite-based electrochemical aptasensor for detection of aflatoxin B1, *Analyst*, 2018, **143**, 1644–1649.

8 S. H. Li, Y. S. MA, Y. K. Lin, G. Xin, M. H. Wang, Z. H. Zhang and Z. Y. Liu, Electrochemical sensor based on a three dimensional nanostructured MoS_2 nanosphere-PANI/reduced graphene oxide composite for simultaneous detection of ascorbic acid, dopamine and uric acid, *RSC Adv.*, 2019, **9**, 2997–3003.

9 R. B. Choudhary and G. Mandal, MoS_2 decorated with graphene and polyaniline nanocomposite as an electron transport layer for OLED applications, *J. Mater. Sci.*, 2020, **31**, 1302–1316.

10 M. J. Shi, Z. Liu, S. Zhang, S. C. Liang, Y. T. Jiang, H. Bai, Z. M. Jiang, J. Chang, J. Feng, W. S. Chen, H. P. Yu, S. X. Liu, T. Wei and Z. J. Fan, A Mott-Schottky Heterogeneous Layer for Li-S Batteries: Enabling Both High Stability and Commercial-Sulfur Utilization, *Adv. Energy Mater.*, 2022, **12**, 2103657.

11 G. H. Gupta, K. Mohan, S. Ghosh, S. S. Babu, R. Velyutham and G. Kapusetti, Label-Free detection of Poly-Cystic Ovarian Syndrome using a highly conductive 2D rGO/MoS_2/PANI nanocomposite based immunosensor, *Bioelectrochemistry*, 2024, **158**, 108681.

12 J. Mariadhas, Y. Subramanian, G. Lakshmanan, F. Hamsath, J. H. R. Monica, M. T. Le, S. S. R. Inbanathan and A. Azad, Emerging robust heterostructure of flower-like (Calendula) MoS_2-warped rGO by polyaniline nanohybrid for antimicrobial and antipollution performances, *Catal. Commun.*, 2024, **187**, 106867.

13 S. Palsaniya, H. B. Nemade and A. K. Dasmahapatra, Synthesis of polyaniline/graphene/MoS_2 nanocomposite for high performance supercapacitor electrode, *Polymer*, 2018, **150**, 150–158.

14 L.-Z. Bai, Y.-H. Wang, S.-S. Cheng, F. Li, Z.-Y. Zhang and Y.-Q. Liu, Synthesis and Electrochemical Performance of Molybdenum Disulfide-Reduced Graphene Oxide-Polyaniline Ternary Composites for Supercapacitors, *Front. Chem.*, 2018, **6**, 218.

15 S. P. Lonkar, V. Gupta, S. M. Alhassan and A. Schiffer, Three-dimensional MoS_x/polyaniline @graphene heteroaerogels as electrode materials for high-performance symmetric supercapacitors, *Energy Storage*, 2023, **5**, e416.

16 M. Baibarac, L. Mihut, G. Louarn, S. Lefrant and I. Baltog, Doping and Metallic-Support Effect Evidenced on SERS Spectra of Polyaniline Thin Films, *J. Polym. Sci., Part B*, 2000, **38**, 2599–2609.

17 M. Scocioreanu, L. Mihut, M. Baibarac and I. Baltog, Photoluminescence decay time studies on ZnS in cubic and hexagonal phase and its mechanico-chemical interaction with polyaniline, *Phys. Status Solidi B*, 2013, **250**, 1426–1431.

18 S. Nawez, Y. Khan, S. Khalid, M. A. Malik and M. Siddiq, Molybdenum disulfide (MoS_2) along with graphene nanoplates (GNPs) utilized to enhance the capacitance of conducting polymers (PANI and PPY), *RSC Adv.*, 2023, **13**, 28785–28797.

19 J. Dai, Y. Luo, J. Zhang, H. Xie, C. Guo, A. Zhu, Y. Xu, M. Fan, C. Yuan and L. Dai, Effect of morphology and phase engineering of MoS2 on electrochemical properties of carbon nanotube/polyaniline @MoS_2 composites, *J. Colloid Interface Sci.*, 2021, **590**, 591–600.

20 H. Ahmad, I. I. Bin Sharfan, R. A. Khan and A. Alsalme, 3D nanoarchitecture of polyaniline – MoS_2 hybrid material for Hg (II) adsorption properties, *Polymers*, 2020, **12**, 2731.

21 M. Madeshwaran, K. S. Rajni and M. Ulaganathan, Polyaniline @MoS_2: An organic and inorganic hybrid framework for asymmetric supercapacitor applications, *Mater. Today Chem.*, 2024, **42**, 102390.

22 C. I. Idumah, A review on polyaniline and graphene nanocomposites for supercapacitors, *Polym.-Plast. Technol. Mater.*, 2022, **61**, 1871–1907.

23 T. Burlanescu, M. Văduva, A. Androne, M. Paraschiv, M. Cercel, C. Negrila and M. Baibarac, Composites based on poly(ortho-toluidine) and reduced graphene oxide: from synthesis to optical characterization and potential applications in the energy storage field, *RSC Adv.*, 2026, **16**(24), 21791–21804.

24 M. Saliba, J. P. Atanas, T. M. Howayek and R. Habchi, Molybdenum disulfide, exfoliation methods and applications to photocatalysis: a review, *Nanoscale Adv.*, 2023, **5**, 6787.

25 S. Quillard, G. Louarn, S. Lefrant and A. G. MacDiarmid, Vibrational analysis of polyaniline: A comparative study of leucoemeraldine, emeraldine, and pernigraniline bases, *Phys. Rev. B:Condens. Matter Mater. Phys.*, 1994, **50**, 12496–12508.

26 M. Lapkowski, K. Berrada, S. Quillard, G. Louarn, S. Lefrant and A. Pron, Electrochemical oxidation of polyaniline in nonaqueous electrolytes – In-situ Raman spectroscopic studies, *Macromolecules*, 1995, **28**, 1233–1238.

27 C. Lee, H. Yan, I. E. Brus, T. E. Heinz, J. Hone and S. Reey, Anamalous lattice vibrations of single and few layer MoS_2, *ACS Nano*, 2010, **4**, 2695–2700.

28 L. M. Malard, M. A. Pimenta, G. Dresselhaus and M. S. Dresselhaus, Raman spectra in graphene, *Phys. Rep.*, 2009, **473**, 51–87.

29 L. G. Cancado, A. Jorio, E. H. Martins Ferreira, F. Stavale, C. A. Achete, R. B. Capaz, M. V. O. Moutinho, A. Lombardo, T. S. Kulmala and A. C. Ferrari, Quantifying defects in graphene via Raman spectroscopy at different excitation energies, *Nano Lett.*, 2011, **11**, 3190–3196.

30 I. Smaranda, A. M. Benito, W. K. Maser, I. Baltog and M. Baibarac, Electrochemical grafting of reduced graphene oxide with polydiphenylamine doped with heteropolyanions and its optical properties, *J. Phys. Chem. C*, 2014, **118**, 25704–25717.

31 M. Baibarac, M. Stroe and S. N. Fejer, Vibrational and photoluminescence properties of polydiphenylamine

doped with silicotungstic acid heteropolyanions and their composites with reduced graphene oxide, *J. Mol. Struct.*, 2019, **1184**, 25.

32 S. Quillard, G. Louarn, J. P. Buisson, S. Lefrant, J. Masters and A. G. MacDiarmid, Vibrational analysis of the reduced form of polyaniline: the leucoemeraldine base, *Synth. Met.*, 1992, **49–50**, 525–530.

33 M. R. Raj, S. Anandan, M. Zhou and M. Ashokkumar, A facil one-step synthesis of hollow polydiphenylamine, *Int. J. Polym. Mater.*, 2013, **62**, 23–27.

34 H. de Santana and F. C. Dias, Characterization and properties of polydiphenylamine electrochemically modified by iodide species, *Mater. Chem. Phys.*, 2003, **82**, 882e886.

35 K. Ataka and M. Osawa, In situ infrared study of water-sulfate coadsorption of gold (111) in sulfuric acid solutions, *Langmuir*, 1998, **14**, 951–959.

36 Z. Ping, G. E. Nauer, H. Neugebauer, J. Theiner and A. Neckel, In situ Fourier transform infrared attenuated total reflection (FTIR-ATR) spectroscopic investigation on the base-acid transitions of leucoemeraldine, *Electrochim. Acta*, 1997, **42**, 1693–1700.

37 M. V. Olenchuk, U. K. Afonina, O. P. Gnatyuk, V. V. Strelchuk, A. S. Nikolenko and G. I. Dovbeshko, Heat annealing influences the optical properties of 2D-MoS_2 nanoparticles, *Mol. Cryst. Liq. Cryst.*, 2022, **749**, 1–8.

38 S. Golczak, A. Kanciurzewska, M. Fahlman, K. Langer and J. J. Langer, Comparative XPS surface study of polyaniline thin films, *Solid State Ionics*, 2008, **178**, 2234–2239.

39 M. M. Mahat, D. Mawad, G. W. Nelson, S. Fearn, R. G. Palgrave, D. J. Payne and M. M. Stevens, Elucidating the protonation of polyaniline films by X-ray photoelectron spectroscopy, *J. Mater. Chem. C*, 2015, **3**, 7180–7186.

40 Y. Zhang, J. Liu, Y. Pan, K. Luo, J. Yu, Y. Zhang, K. Jla, H. Yln, H. Tlan and Z. Wu, The evolution of MoS2 properties under oxygen plasma treatment and its application in MoS_2 based devices, *J. Mater. Sci.:Mater. Electron.*, 2019, **30**, 18185–18190.

41 N. H. Turmer and A. M. Singlet, Determination of peak position and areas from wide-scan XPS spectra, *Surf. Interface Anal.*, 1990, **15**, 215–222.

42 A. A. Salem and B. N. Grgur, The influence of the polyaniline initial oxidation states on the corrosion of steel with composite coatings, *Prog. Org. Coat.*, 2018, **119**, 138–144.

43 P. J. Dysona and P. G. Jessopb, Solvent effects in catalysis: rational improvements of catalysts via manipulation of solvent interactions, *Catal. Sci. Technol.*, 2016, **6**, 3302.

44 M. Isanejad, N. Azizi and T. Mohammadi, Pebax membrane for CO_2/CH_4 separation: Effects of various solvents on morphology and performance, *J. Appl. Polym. Sci.*, 2017, **134**(9), 44531.

45 P. Kumar, S. Verma, R. Kaur, J. Papac, H. Kusic and U. L. Stangar, Enhanced photo-degradation of N-methyl-2-pyrrolidone (NM): influence of matrix components, kinetic study and artificial neural network modelling, *J. Hazard. Mater.*, 2022, **434**, 128807.

46 A. S. Farooqi, R. M. Ramii, S. S. M. Lock, A. S. Farooqi, M. Z. Shahid, S. M. W. Hasmain, N. Hira and B. Abdullah, Removal of carbon dioxide and hydrogen sulfide from natural gas using a hybrid solvent of monoethanolamine and N-methyl-2-pyrrolidone, *ACS Omega*, 2024, **4**, 25704–25714.